A genetic algorithm-based method for the mechanical characterization of biosamples using a MEMS microgripper: numerical simulations

M. Verotti [1a], P. Di Giamberardino[b], N. P. Belfiore[c], O. Giannini[d]

[a] *Department of Mechanical, Energy, Management and Transportation Engineering, University of Genoa, 16145 Genoa, Italy.*
[b] *Department of Computer, Control and Management Engineering Antonio Ruberti, Sapienza University of Rome, 00185 Rome, Italy*
[c] *Department of Engineering, Roma Tre University, 00100 Rome, Italy*
[d] *Niccolò Cusano University, 00166 Rome, Italy*

Abstract

In this paper, the viscoelastic characterization of biosamples is addressed considering a measuring technique relying on the use of a MEMS techonology-based microgripper. A proper mechanical model is developed for the coupled nonlinear dynamics of the microsystem, composed of the measuring tool and the specimen to be analyzed. The Maxwell liquid drop model and the generalized Maxwell-Wiechert model are considered for the sample, and the identification of the viscoelastic parameters is performed by implementing a genetic algorithm.

Keywords: MEMS Microgripper, Micromanipulation, Biosamples Analysis, Viscoelastic Characterization, Parameters Estimation, Genetic Algorithms

1. Introduction

The identification of the mechanical characteristics of tissues, cells, and, more in general, natural and synthetic biomaterials, plays an important role in many research fields, such as biology, regenerative medicine, and diagnosis of diseases. Mechanical characterization of biosamples is necessary for understanding the role of material mechanics in disease diagnosis or progression (Mijailovic

[1] Corresponding author. Address: Department of Mechanical, Energy, Management and Transportation Engineering, University of Genoa, Via all'Opera Pia, 15, 16145 Genoa, Italy. E-mail: matteo.verotti@unige.it

et al., 2018), replacing or mimicking tissues (Backman et al., 2017), and, more in general, for validating the constitutive models and the simulation results (Zhang et al., 2018).

For example, characterization of brain and brain-skull interface tissues (Wang et al., 2018) is fundamental in modeling and understanding the mechanics of traumatic brain injury (Zhang et al., 2018), blast–induced neurotrauma (Laksari et al., 2015), and brain shift (Forte et al., 2018). Current investigations show that brain tissue is anisotropic, non-linear, viscoelastic (Jin et al., 2013), and that the constitutive relations obtained for a specific loading condition could not predict the response for other loads (Miller and Chinzei, 2002). In regenerative medicine bone scaffolds, used to guide and stimulate tissue growth, are subjected to mechanical stresses. Therefore, before implantation, it is necessary to determine whether their mechanical properties meet the specified requirements (Vivanco et al., 2012; Prasadh and Wong, 2018).

Besides the studies on brain tissues and scaffolds, characterization and constitutive modeling of skeletal muscle (Marcucci et al., 2017; Garcés-Schröder et al., 2018), skin (Sherman et al., 2017; Hsu et al., 2018), lung (Freed and Einstein, 2012), blood vessels (Backman et al., 2017), pericardium (Murdock et al., 2018), articular cartilage (Marchi and Arruda, 2017), vocal fold (Erath et al., 2017), and cornea (Whitford et al., 2018) tissues have also been the subjects of extensive research efforts. It is worth noting that tissue stiffening is a hallmark of several disease states, including fibrosis and some types of cancers (Pogoda et al., 2014). Regarding the circulatory system, vascular stiffness affects blood pressure, permeability, and inflammation, driving diseases such as pulmonary arterial hypertension, kidney disease, and atherosclerosis (Huveneers et al., 2015). While diseases grow to impair the function of tissues in an organism, their initiation and development starts within individual cells. In fact, biological materials are characterized by many levels of structures, from the macroscopic to the microscopic scale, and their properties arise from coordinated processes across this hierarchical architecture (Weiner and Wagner, 1998; Ji and Gao, 2004).

Since heterogeneity in cell populations has been demonstrated, the understanding of individual cells behavior represents a significant challenge (Altschuler and Wu, 2010). Cells have demonstrated sensitivity to biochemical and mechanical stimulation: their mechanical properties change in accordance with their functional state or in response to external stimuli. More specifically, cells can reinforce or fluidize their cytoskeletons through polymerization of their filamentous proteins, varying their structural stiffness. Cells can also generate physical forces to interact with their physical environment. Mechanical cues or abnormal environments can disturb their normal function, and disease states can arise. Asthma, osteoporosis, deafness, atherosclerosis, cancer, osteoarthritis, glaucoma, muscular dystrophy, and pressure ulcers can be directly caused by or catalyzed by irregular cell mechanics (Rodriguez et al., 2013; Rodriguez and Sniadecki, 2014; Ingber, 2003). Therefore, mechanical characterization of single cells can provide useful information about these processes.

For example, a strong association between cell stiffness and invasive potential in pancreatic ductal adenocarcinoma cells (PDAC) was reported in (Nguyen et al., 2016), finding that stiffer PDAC cells are more invasive than more compliant cells. Moreover, while progress has been made in understanding molecular mechanisms of breast cancer progression, characterization of the associated cellular mechanical properties remains incomplete (Baker et al., 2010). Stiffness determination represents a key aspect, because breast tumors are stiffer than normal breast tissue, and cancer cell motility depends on the stiffness of the extracellular matrix. On the other hand, more deformable cell may have a selective advantage for metastasis (Nguyen et al., 2016). It has been showed that ovarian cancer cells are generally softer and display lower intrinsic variability in cell stiffness than non-malignant ovarian epithelial cells (Xu et al., 2012). Besides stiffness, also viscosity can potentially be considered as a biomarker for evaluating the metastatic potential of cancer cells (Hu et al., 2017). As reported in (Zouaoui et al., 2017), the analysis of viscosity showed that healthy cells are more viscous compared to metastatic cells. Furthermore, considering both elastic and viscous properties may be more effective in distinguishing specific

diseases (Rubiano et al., 2018).

The experimental techniques for investigating cell mechanics can be generally classified in force-application and force-sensing techniques. According to the force-application techniques, a force is applied to the cell and its response (mechanical and/or biochemical) is recorded. These methods include micropipette aspiration, microneedle and atomic force microscope probing (Buffinton et al., 2015; Eng and Sampathkumar, 2018), optical trapping, magnetic twisting cytometry, substrate strain. In force-sensing techniques, cells are seeded onto deformable structures and traction forces are measured. Traction force microscopy, wrinkling membranes and micropost arrays belong to this category. The selection of the proper technique depends on several factors, such as size of the biological sample and feature to be acquired. Each one of these methods has its own advantages and disadvantages, in terms of spatial and force resolution, accuracy, detrimental effects on cell, transferability of results (Addae-Mensah and Wikswo, 2008; Rodriguez et al., 2013).

Given the variety of experimental techniques, many mechanical models have been proposed in literature, generally considering two different approaches. By following the micro/nanostructural approach, several cytoskeletal models for adherent cells have been derived, such as tensegrity model, tensed cable networks, open-cell foam model. According to this approach, the cytoskeleton is the main structural component. According to the continuum approach, the cell is considered as a continuum material, and appropriate constitutive models and related parameters have to be experimentally determined. Many models have been proposed in literature: biphasic model, liquid drop models (Newtonian, Compound Newtonian, Shear thinning, Maxwell), solid viscoelastic models (Kelvin-Voigt, Maxwell, Zener) (Chen et al., 2012; Lim et al., 2006). Results obtained at the cell level can be useful in understanding the stress and strain distribution and the mechanism of force transmission to the cytoskeleton. Therefore, the method can serve as a basis for further studies at the sub-cell level.

After the model has been defined, the mechanical characterization of the biosample can be formulated as a parameter estimation problem, where the

unknowns to be identified are the stiffness and damping coefficients of the determined model. Hence, the estimation problem can be solved by using least-squares (Johnson and Faunt, 1992) or Kalman filtering (Xi et al., 2011) methods. Other solution approaches makes use of inverse finite element method (Boonvisut and Çavuşoğlu, 2013; Kauer et al., 2002) or genetic algorithms (Belfiore and Esposito, 1998; Kohandel et al., 2008; Chawla et al., 2009).

Recently, considering the increasing use of microgrippers for the manipulation at the microscale (Verotti et al., 2017a; Dochshanov et al., 2017), a novel technique for the viscoelastic characterization of soft materials was presented by the Authors (Di Giamberardino et al., 2018). The proposed method resorted to the use of a MEMS microgripper and to a control system based on a standard PID regulator. According to the measurement technique, starting from the initial symmetric configuration, one arm was actuated to grip the sample, whereas the other one served as sensing element. During the gripping task, the actuated arm drove the sample towards the sensing arm, causing its displacement from the neutral configuration. Therefore, the loss of the symmetry condition was exploited to perform the measurement. The developed mechanical model considered the coupled nonlinear dynamics of the microgripper-sample system and the Kelvin-Voigt constitutive law of viscoelasticity for the specimen.

In this investigation, a novel method is presented to perform the measurement task by using the MEMS microgripper. The strategy preserves the symmetric condition with the simultaneous actuation both the gripping arms. Furthermore, two different constitutive models and a new solution method are proposed for the technique presented in (Di Giamberardino et al., 2018). More specifically, the Maxwell liquid drop model and the generalized Maxwell-Wiechert model are considered for the sample, and the estimation problem is solved by implementing a genetic algorithm. The work is organized as follows. The experimental technique and the mechanical models are presented in Sections 2 and 3, respectively. The solution approach is described in Section 4, whereas the results are presented and discussed in Section 5.

2. Experimental technique

The experimental technique adopted for the viscoelastic characterization of the biosamples resorts to the use of the MEMS technology-based microgripper shown in Figures 1 and 2. The gripper consists of a compliant silicon structure fabricated by applying the deep reactive-ion etching process on silicon-on-insulator wafers (Bagolini et al., 2017). Each gripper arm is actuated by a rotary comb drive, and the connection between the movable part and the anchored part is achieved by means of the conjugate surfaces flexure hinge (CSFH) (Verotti et al., 2015). During the actuation process, the deflections of the flexible elements allow the arms to rotate, performing the gripping task (Cecchi et al., 2015). Due to the electrostatic-based actuation system, the motion plane of the gripper arms can be arranged perpendicularly or with an inclined angle with respect to the sample support plane, in order to avoid the submersion of the device in liquid environment.

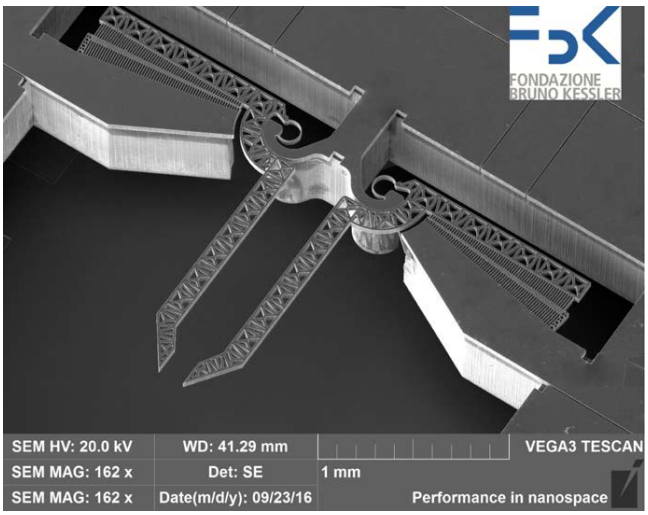

Figure 1: SEM image of the silicon microgripper.

According to the measurement procedure presented in (Di Giamberardino et al., 2018), the left arm of the device is actuated to grip the sample between the jaws until the right arm reaches a predefined rotation. This angular displace-

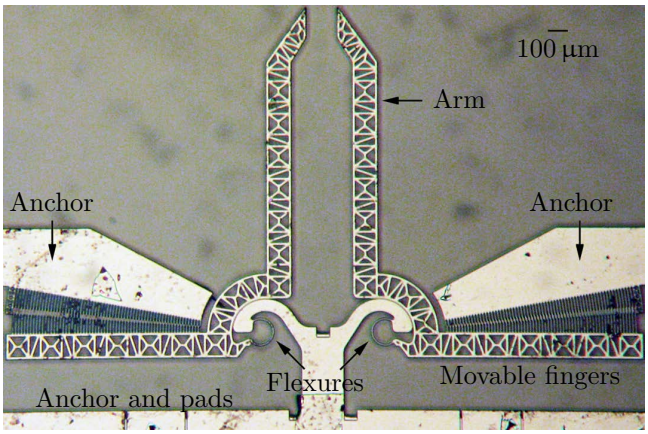

Figure 2: Optical microscope image of the silicon microgripper.

ment serves as reference signal for the implemented feedback control system. Therefore, the elastic coefficient of the sample can be computed at steady state conditions, whereas its viscosity parameter can be obtained as a function of the input torque frequency by adding a small-amplitude sinusoidal signal to the left arm. It is worth noting that during the measurement procedure the microgripper modifies its neutral symmetric configuration to an asymmetric one.

In the present investigation, it is assumed that a control torque is exerted by each comb drive in order to grip the cell sample. The actuation system is therefore symmetric, and the microgripper changes its configurations preserving the symmetry condition. This feature entails some advantages from the modeling and from the operational points of view. Considering the modeling aspect, the kinematics of the system is simpler than in the previous case, and can be represented by a simpler model. Considering the operational aspect, a unique input signal can be set to actuate the system. The rotation of at least one of the two arms is supposed to be measured, whereas the mechanical characteristics of the sample are supposed to be unknown.

The exciting torques, as it can be seen in Figure 3, are applied into two phases: (i) torque application and (ii) relaxation. During the first phase that last 200 s, a 1.6×10^{-3}µNm torque is applied to grip the sample. This value

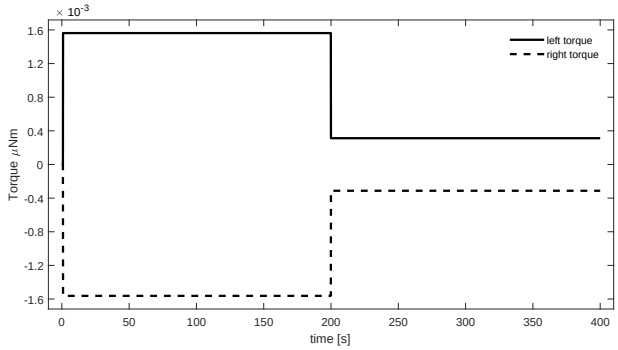

Figure 3: Evolution of the applied torques

corresponds to an electric potential difference applied to the comb drive pads of about 17 V, as detailed in Section 3. During the second phase that last the following 200 s, the torque is reduced down to one-fifth of the initial value, that is 0.32×10^{-3}μNm, in order to maintain the grip with the sample. The rotation of one arm is recorded throughout the 400 s gripping time, and it is assumed that a 10% random noise is present on the measured rotation response.

According to the proposed design, the distance between the jaws in neutral configuration is equal to 150 μm. This distance allow the adoption of the microgripper for the manipulation of samples with characteristic length belonging to the range [30,120]μm. However, due to the symmetric configuration of the system, this parameter can be easily set-up during the design stage without affecting the results hereafter presented. In fact, the gripper capability to determine the sample mechanics depends on the elastic properties of the device and on the implemented algorithm used for the identification, which must be robust with respect to the measurement noise.

It is worth noting that, by taking advantage of the device sensing and actuation arrangement, the model parameters of each jaw can be obtained during pre-operative procedures. More specifically, the stiffness and damping coefficients (k_i, c_i, $i = \{2, 4\}$, see Section 3) can be determined considering a standard impulse or a step response in case of no load conditions (i.e. operating the gripper arms with no samples) (Ewins, 2009). From this test it is also possible

to calibrate the model for the specific device in order to offset any parameter variation due to the fabrication process.

3. Mechanical model

The compliant structure of the microgripper is schematically represented in Figure 4 where, in operative condition, the specimen is in contact to the tweezers tips at the points B and C. The points A and D represent the centers of rotation (Verotti, 2018) of the left and right arms of the gripper, respectively. According to the rigid-body replacement method (Sanò et al., 2018), a pseudo-rigid body model (PRBM) can be obtained from the compliant structure by substituting the constant-curvature CSFHs with revolute joints (Verotti et al., 2017b).

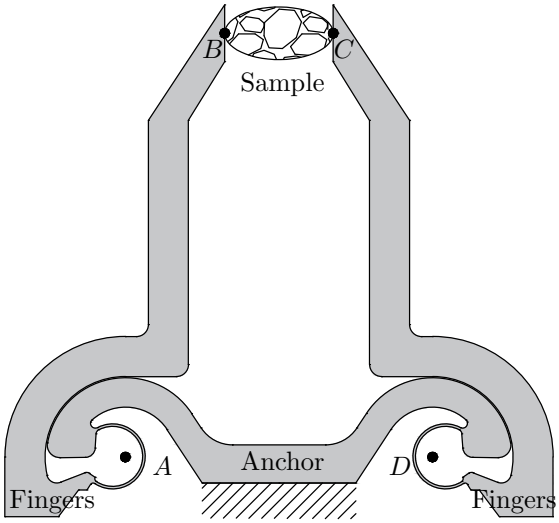

Figure 4: Operational condition and schematic representation of the compliant structure of the microgripper

The PRBM, consisting of the closed chain $ABCD$, is illustrated in Figure 5. The link AD and the links AB, DC, with fixed lengths, correspond to the frame and to the gripper arms, respectively. The link BC represents the biosample and, according to the measurement procedure, it is characterized by a variable length. As depicted in Figure 5, the Maxwell liquid drop model with mem-

brane stiffness and the generalized Maxwell-Wiechert model are considered as constitutive models for the specimen.

The system configuration can be described by means of reference, target and incremental variables, as represented in Figure 6. The reference variables ($\hat{v}$) define the system in the symmetrical configuration, where the gripper arms are in contact to the sample but no deformations occur. The target variables ($\tilde{v}$) define the system in the deformed configuration. Therefore, the incremental variables are defined as $v = \tilde{v} - \hat{v}$. The model parameters are listed and defined in Table 1.

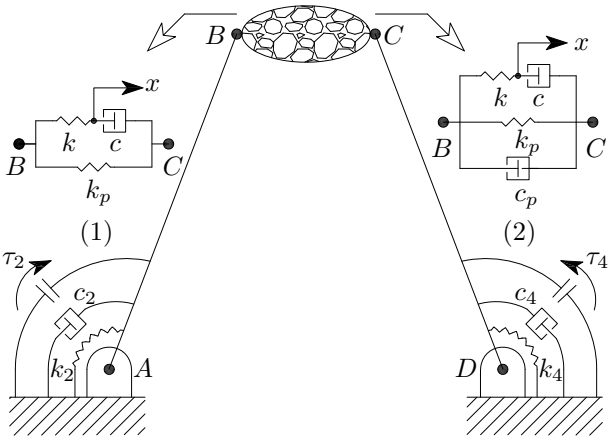

Figure 5: Pseudo-rigid body model of the microgripper and constitutive models of linear viscoelasticity: Maxwell liquid drop with membrane stiffness (1) and generalized Maxwell (2) models.

Assuming the inertia of the sample to be negligible, the dynamical model of the system can be described by means of the following equations,

$$\begin{aligned} & I_2\ddot{\theta}_2 + c_2\dot{\theta}_2 + c_p l^2 \left[\dot{\theta}_2 \sin\tilde{\theta}_2 - \dot{\theta}_4 \sin\left(\pi - \tilde{\theta}_4\right)\right] \sin\tilde{\theta}_2 \\ & + k_2\theta_2 - kl\left[l\left(\cos\tilde{\theta}_2 - \cos\hat{\theta}_2\right) - x\right] \sin\tilde{\theta}_2 \\ & - k_p l^2 \left(\cos\tilde{\theta}_2 - \cos\hat{\theta}_2 - \cos\tilde{\theta}_4 + \cos\hat{\theta}_4\right) \sin\tilde{\theta}_2 = \tau_2, \end{aligned} \tag{1}$$

Table 1: Nomenclature and parameters values

Par.	Unit	Value	Definition
d	[m]	5.47e−4	length of AD
l	[m]	1.50e−3	length of AB and DC
$\hat{u}$,	[m]	150e−6	reference length of BC
$\hat{\theta}_2$	[rad]	1.44	reference orientation of AB
$\hat{\theta}_4$	[rad]	1.70	reference orientation of DC
k_2, k_4	[Nm]	0.30e−6	left and right arm torsional stiffness
c_2, c_4	[Nsm]	1.24e−12	damping coefficients of the gripper arms
I_2, I_4	[kgm^2]	1.25e−14	left and right arm moments of inertia
$\tilde{u}$, u	[m]		target and incremental lengths of BC
$\tilde{\theta}_2$, θ_2	[rad]		target and incremental orientations of AB
$\tilde{\theta}_4$, θ_4	[rad]		target and incremental orientations of DC
τ_2, τ_4	[Nm]		left and right comb drive input torques
k, k_p	[Nm^{-1}]		stiffness coefficients of the sample
c, c_p	[Nsm^{-1}]		damping coefficients of the sample

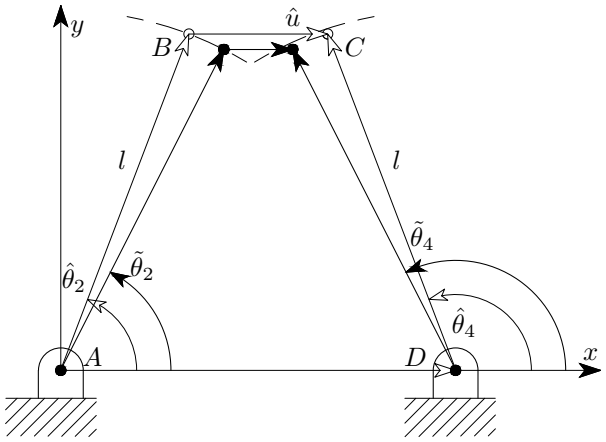

Figure 6: Nomenclature and model parameters in neutral (soft lines) and general (hard lines) configurations.

$$
\begin{aligned}
&I_4\ddot{\theta}_4 + c_4\dot{\theta}_4 + cl^2\left[\dot{\theta}_4 \sin\left(\pi - \tilde{\theta}_4\right) - \dot{x}\right]\sin\tilde{\theta}_4 + k_4\theta_4 \\
&-c_p l^2\left[\dot{\theta}_2 \sin\tilde{\theta}_2 - \dot{\theta}_4 \sin\left(\pi - \hat{\theta}_4\right)\right]\sin\left(\pi - \tilde{\theta}_4\right) \\
&+k_p l^2\left(\cos\tilde{\theta}_2 - \cos\hat{\theta}_2 - \cos\tilde{\theta}_4 + \cos\hat{\theta}_4\right)\sin\left(\pi - \tilde{\theta}_4\right) = \tau_4,
\end{aligned} \tag{2}
$$

$$
k\left[l\left(\cos\tilde{\theta}_2 + \cos\hat{\theta}_2\right) + x\right] + c\left(l\sin\tilde{\theta}_4\ \dot{\tilde{\theta}}_4 - \dot{x}\right) = 0, \tag{3}
$$

representing the dynamic equilibrium of the left arm, the right arm and the sample, respectively. From the previous nonlinear system, an approximate linear set of equations can be obtained around the reference configuration. By assuming $\theta_2 \ll 1$ and $\theta_4 \ll 1$, which implies $\tilde{\theta}_2 \simeq \hat{\theta}_2$ and $\tilde{\theta}_4 \simeq \hat{\theta}_4$, respectively, it follows

$$
\begin{aligned}
&I_2\ddot{\theta}_2 + c_2\dot{\theta}_2 + c_p l^2\left(\dot{\theta}_2 \sin\hat{\theta}_2 - \dot{\theta}_4 \sin\hat{\theta}_4\right)\sin\hat{\theta}_2 \\
&+k_2\theta_2 + kl\left(l\theta_2 \sin\hat{\theta}_2 - x\right)\sin\hat{\theta}_2 \\
&+k_p l^2\left(\theta_2 \sin\hat{\theta}_2 - \theta_4 \sin\hat{\theta}_4\right)\sin\hat{\theta}_2 = \tau_2,
\end{aligned} \tag{4}
$$

$$
\begin{aligned}
&I_4\ddot{\theta}_4 + c_4\dot{\theta}_4 + cl^2\left[\dot{\theta}_4 \sin\hat{\theta}_4 - \dot{x}\right]\sin\hat{\theta}_4 + k_4\theta_4 \\
&-c_p l^2\left[\dot{\theta}_2 \sin\hat{\theta}_2 - \dot{\theta}_4 \sin\hat{\theta}_4\right]\sin\hat{\theta}_4 \\
&+k_p l^2\left(\theta_2 - \sin\hat{\theta}_2 + \theta_4 + \sin\hat{\theta}_4\right)\sin\hat{\theta}_4 = \tau_4,
\end{aligned} \tag{5}
$$

$$
k\left(l\theta_2 \sin\hat{\theta}_2 - x\right) + c\left(\dot{x} - l\dot{\theta}_4 \sin\hat{\theta}_4\ \right) = 0. \tag{6}
$$

The system (4)-(6) is a system of second order linear differential equations with three state variables: θ_2, θ_4, and x. The linear coefficients depend nonlinearly on the system configuration that can be measured (i.e. $\hat{\theta}_2$ and $\hat{\theta}_4$).

The relations among torque, capacitance, and angular position can be determined with reference to Figure 7. The capacitance of the comb drive C_t can be calculated as (Chang et al., 2014; Di Giamberardino et al., 2018):

$$
C_T = \epsilon_0 h\theta\left[\sum_{i=1}^{n-1}\left[\ln A\right]^{-1} + \sum_{i=0}^{n-1}\left[\ln B\right]^{-1}\right], \tag{7}
$$

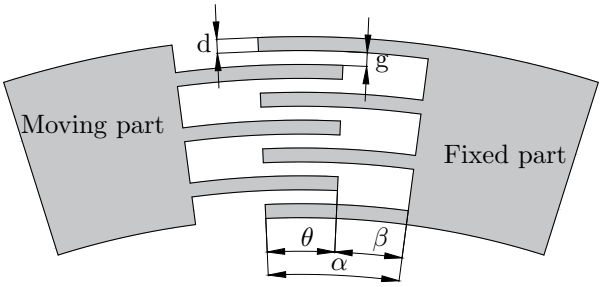

Figure 7: Geometric parameters of the comb-drive actuator.

where

$$A = \frac{r_0 + 2i(d+g)}{r_0 + 2i(d+g) - g}\,,$$
$$B = \frac{r_0 + (2i+1)(d+g)}{r_0 + 2i(d+g) + d}\,.$$

In eqn.(7), ϵ_0 is the vacuum permittivity, h is the thickness of the device layer, θ is the overlap angle, n is the number of fingers, r_0 is the radius of the first finger, and d is the finger width.

The corresponding electrostatic torque can be determined as

$$\tau = \frac{1}{2}\left(\frac{\partial C_T}{\partial \theta}\right) V^2\,, \tag{8}$$

where V is the applied voltage. Substituting eqn.(7) in eqn.(8), it follows

$$\tau = \frac{1}{2}\epsilon_0 h V^2 \left[\sum_{i=1}^{n-1} [\ln A]^{-1} + \sum_{i=0}^{n-1} [\ln B]^{-1}\right]. \tag{9}$$

Table 2 lists the values of the geometric parameters of the actuator. According to the reported values, the voltage corresponding to the input torque of 1.6 μNm is about 17 V, whereas the applied voltage corresponding to the reduced torque value of 0.32 μNm is about 7 V.

4. Solution of the estimation problem: genetic algorithm implementation

Genetic algorithms are non derivative methods for global optimization based on the principles of genetics and natural selection, widely used in many research

Table 2: Geometric parameters of the comb drive actuator

Geometric parameter	label	Value
Thickness of the device layer	h	40 µm
Finger width	d	4 µm
Finger gap	g	3 µm
Number of floating fingers	n	66
Finger angle	α	6°
Finger stroke	β	4.50°
Finger initial overlap	θ	1.50°
Radius of the first finger	r_0	321µm

fields because of their many advantages, such as robustness, efficiency, and capability to deal with a large number of variables (Haupt and Haupt, 1998). Genetic algorithms procedure generally consists of four steps (Dao et al., 2017), that are initialization, crossover, selection and mutation. Genetic coding of parameters and formulation of fitness function have also to be considered in the algorithm implementation.

A chromosome encodes the data defining an *individual cell model* within a population. How to encode the model data in the chromosome is one of the first choices to make in order to implement a genetic algorithm. The principal types of encoding are binary, permutation, value, and tree. In this study, the value encoding is used, in which each chromosome is a set of real numbers properly encoded within a give number of bits. More specifically, it is required to encode four independent parameters: the stiffness coefficients k and k_p, and the damping coefficients c and c_p (phenotype). Each one of these values is encoded into the chromosome (genotype) using three independent genes, one defining the order of magnitude, and the other two genes defining the first two

significant digits of the parameter, as:

$$\begin{aligned} k &= 10^{g_{k_1}} \left(0.1 g_{k_2} + 0.01 g_{k_3}\right), \\ k_p &= 10^{g_{k_{p1}}} \left(0.1 g_{k_{p2}} + 0.01 g_{k_{p3}}\right), \\ c &= 10^{g_{c_1}} \left(0.1 g_{c_2} + 0.01 g_{c_3}\right), \\ c_p &= 10^{g_{c_{p1}}} \left(0.1 g_{c_{p2}} + 0.01 g_{c_{p3}}\right). \end{aligned} \tag{10}$$

The adopted choice of splitting each parameter among three independent genes allows a faster convergence of the algorithm while allowing a large span in each parameter range and fixed precision (Zhou et al., 2017). Each gene in eqn. 10 may assume the values reported in Table 3. Therefore, the chromosome set is

$$\{g_{k_1}, g_{k_2}, g_{k_3}, g_{k_{p1}}, g_{k_{p2}}, g_{k_{p3}}, g_{c_1}, g_{c_2}, g_{c_3}, g_{c_{p1}}, g_{c_{p2}}, g_{c_{p3}}\}.$$

The set is characterized by 12 integer genes, and each one of them can assume few possible values (either 9 or 12, see Table 3). The physical values of each parameter may therefore range as reported in Table 4, with two significant digits.

Table 3: Possible values for each gene

Gene	Min	Max	Steps
g_{k_1}	-3	8	12
$g_{k_{p1}}$	-3	8	12
g_{c_1}	-4	5	12
$g_{c_{p1}}$	-4	5	12
g_{k_2}, $g_{k_{p2}}$, g_{c_2}, $g_{c_{p2}}$	1	9	9
g_{k_3}, $g_{k_{p3}}$, g_{c_3}, $g_{c_{p3}}$	1	9	9

It is worth noting that the proposed algorithm does not assume the order of magnitude of each parameter value known *a priori*, that is indeed provided by the identification procedure. The initial population of models, set to 500 individuals, is generated by assigning to each gene a random value within the

Table 4: Model parameters: ranges of values

Gene	Unit	Min	Max
k	[Nm^{-1}]	1.1e−4	9.9e+7
k_p	[Nm^{-1}]	1.1e−4	9.9e+7
c	[Nsm^{-1}]	1.1e−5	9.9e+4
c_p	[Nsm^{-1}]	1.1e−5	9.9e+4

range reported in Table 3. The population evolves into the next generation by three genetic operators: crossover (i), mutation (ii) and selection (iii).

The crossover (i) is performed between two selected individuals, called parents, by exchanging parts of their genetic strings, which start from a randomly chosen crossover point. Among the crossover types, in this study, the single-point crossover is considered and the site for the crossover operation is selected randomly on each chromosome.

The mutation (ii) is used to avoid local convergence of the algorithm (Esen and Koç, 2015) by introducing random variation in the genome of some individuals. As the generations number increases, chromosomes become similar to each other, even if a high crossover rate is determined. This situation blocks diversity and prevents the occurrence of more powerful generations. For this purpose, the mutation operator is used to increase diversity of chromosome in population by altering one or more genes. In particular, the mutation operator starts only after some new generations (at 20^{th}, generation) with a fixed probability of occurrence, which in this case is set at 50%. A single-point mutation is considered and the site for the mutation operation is selected randomly on each chromosome.

The selection operator (iii) decides which chromosome will be transferred to the next generation and which one will be eliminated, by using selection probabilities of each chromosome. Several methods such as roulette-wheel, ranking, tournament, and sharing, have been introduced for selecting genomes. In this investigation, the ranking method was adopted. The selection of the individuals

takes place through sorting accordingly to their fitness values obtained using an objective function. Rank selection first ranks the population and then every chromosome receives fitness from this ranking. The worst will have fitness 1, second worst 2, etc., and the best will have fitness N (number of chromosomes in population). Therefore, the best 50% of the population (250 individuals) are kept in the next generation and are chosen to mate. These individuals generate, through the crossover operator, 250 new individuals that take the place of the lowest 50% of the population being discarded.

5. Simulations and results

In this study, the cell model is generated for each individual in the population transcoding the parameter values, according to eqn. 10. A dynamic simulation of the system, in operative condition, is performed in order to acquire the time history of the left arm rotation (θ_2), and to compared it to the target one (supposedly measured, i.e θ_2^m). For each individual, the fitness function is the root mean square of the difference between the simulated dynamic response of the system and the reference one. Throught the generations, the fitness value of the most fit individual increases, reaching a stationary value. Hence, the genetic algorithm stops and the fittest individual is selected as *optimal solution*. Generally, convergence is reached around the 60^{th} generation. Further 20 generations are computed to verify if mutation can move the optimum from a local minimum toward a better solution, as depicted in Figure 8.

In order to test the capability of the GA in identifying the dynamic parameters of the sample, the first numerical simulation is performed by considering a cell model characterized by linear viscoelastic behavior defined by the parameters values listed in Table 5. The values are adapted from Refs.(Lim et al., 2006; Sato et al., 1990) for the case of endothelial cells (T^{c}) The dynamics of the system is driven by k, k_p and c, whereas the low value of c_p does not affect the evolution. A comparison between the target response of the system and the best fit solution, obtained at the 70^{th} generation, is reported in Figure 9. Figure 10

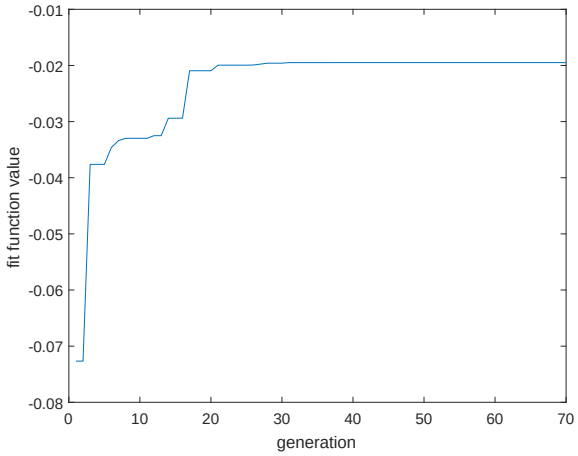

Figure 8: Convergence of the genetic algorithm

Table 5: Linear viscoelastic model: comparison of target and identified values

Parameter	Unit	Target	Identified	Error [%]
k	$[\mathrm{Nm}^{-1}]$	35.0	32.8	6.1
k_p	$[\mathrm{Nm}^{-1}]$	12.3	12.3	0
c	$[\mathrm{Nsm}^{-1}]$	299.9	302.5	-0.8
c_p	$[\mathrm{Nsm}^{-1}]$	1e$-$3	1e$-$4	> 100

shows the evolution throughout generations of the cell dynamic parameter. It can be noticed how, except c_p, the order of magnitude of the parameters that have a large effect on the solution is obtained around the 20^{th} generation. The numerical comparison between identified and reference values in Table 5 shows that k_p and c have a negligible error, whereas the error on k is lower than the noise level added to the reference signal. The exact value of c_p is not precisely identified, but the results highlight that it has a very low value that does not affect the response of the system.

The identification process is generally able to perform the estimation procedure also in case of simpler models, such as the Maxwell liquid drop model

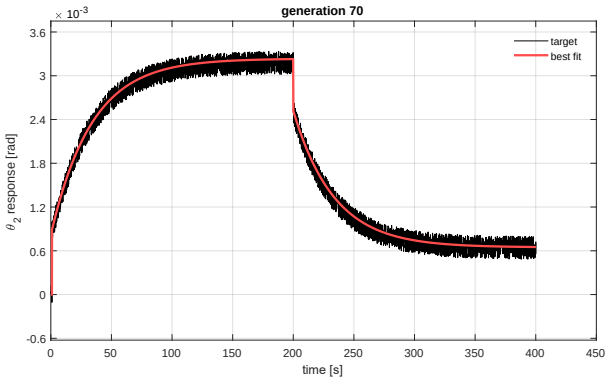

Figure 9: Linear viscoelastic model: comparisons between the response of the system and the best fit solution obtained with the GA

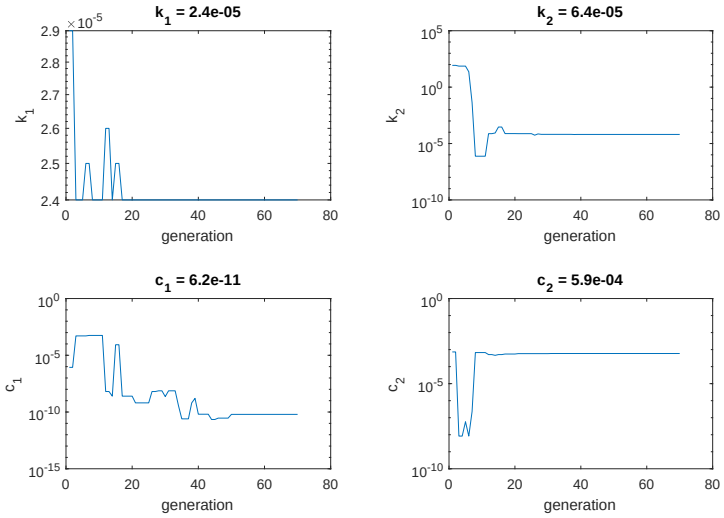

Figure 10: Linear viscoelastic model: evolution of the best fit parameters values throughout generations

with cell membrane stiffness, where, with respect to the generalized Maxwell-Wiechert model, k_p and c_p have negligible values. The system response, for the numerical parameter listed in Table 6 (case 1), is dominated basically by the damping value. The genetic algorithm fits correctly the response (Figure 11), and it is able to identify with small error the key parameter c, and to catch k_p

and k orders of magnitude.

Table 6: Liquid drop model (case 1): comparison of target and identified values

Parameter	Unit	Target	Identified	Error [%]
k	$[\mathrm{Nm}^{-1}]$	9.5	6.7	29
k_p	$[\mathrm{Nm}^{-1}]$	1e−4	5.6e−5	44.0
c	$[\mathrm{Nsm}^{-1}]$	10	9.7	2.6
c_p	$[\mathrm{Nsm}^{-1}]$	1e−4	0.23	> 100

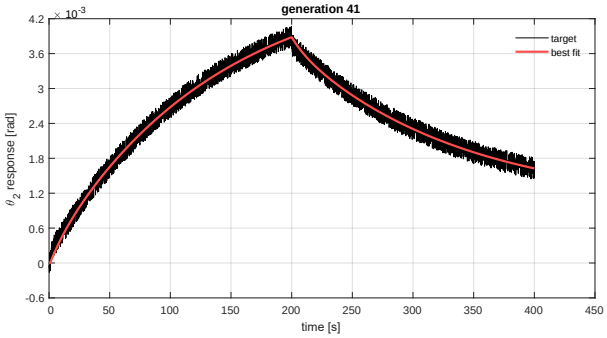

Figure 11: Liquid-drop model (case 1): comparisons of system response and best fit solution obtained with the GA

The case corresponding to a lower value of k ($1\,\mathrm{Nm}^{-1}$, case 2) is reported in Figure 12, The response becomes affected by the k value, thus the identification improves performing a good identification for k and c, (error below 3%), as shown in Table 7.

6. Conclusions

In this paper, a novel experimental technique, based on the use of a MEMS microgripper, has been introduced in order to evaluate the mechanical characteristics of biomaterials. A genetic algorithm has been implemented to solve the parameter estimation problem. The simulations results confirm the feasibility of the approach for the Maxwell liquid drop and the generalized Maxwell-Wiechert

Table 7: Liquid-drop model (case 2): comparison of target and identified values

Parameter	Unit	Target	Identified	Error [%]
k	$[\mathrm{Nm}^{-1}]$	1	0.97	2.6
k_p	$[\mathrm{Nm}^{-1}]$	1e−4	5.6e−5	44.0
c	$[\mathrm{Nsm}^{-1}]$	10	9.7	2.6
c_p	$[\mathrm{Nsm}^{-1}]$	1e−3	0.25	> 100

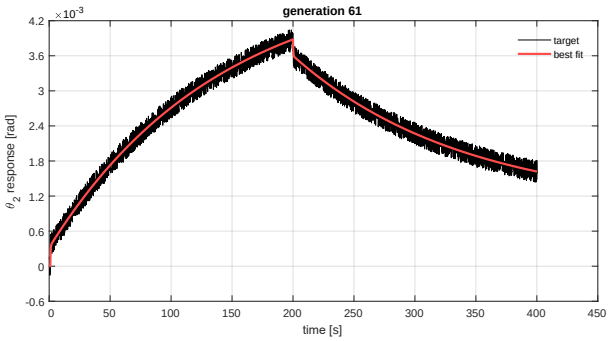

Figure 12: Liquid drop model (case 2): comparisons of system response and best fit solution obtained with the GA

constitutive models adopted for the sample. The proposed technique appears to be highly robust with respect to measurement noise and does not require to assume a priori the order of magnitude of the parameter to be identified nor the specific cell model.

References

Addae-Mensah, K.A., Wikswo, J.P., 2008. Measurement techniques for cellular biomechanics in vitro. Experimental biology and medicine 233, 792–809.

Altschuler, S.J., Wu, L.F., 2010. Cellular heterogeneity: do differences make a difference? Cell 141, 559–563.

Backman, D.E., LeSavage, B.L., Shah, S.B., Wong, J.Y., 2017. A robust method

to generate mechanically anisotropic vascular smooth muscle cell sheets for vascular tissue engineering. Macromolecular bioscience 17.

Bagolini, A., Ronchin, S., Bellutti, P., Chiste, M., Verotti, M., Belfiore, N., 2017. Fabrication of novel mems microgrippers by deep reactive ion etching with metal hard mask. IEEE J. Microelectromechanical Syst. 26, 926 – 934.

Baker, E.L., Lu, J., Yu, D., Bonnecaze, R.T., Zaman, M.H., 2010. Cancer cell stiffness: integrated roles of three-dimensional matrix stiffness and transforming potential. Biophysical journal 99, 2048–2057.

Belfiore, N.P., Esposito, A., 1998. Theoretical and experimental study of crossover operators of genetic algorithms. Journal of Optimization Theory and Applications 99, 271–302.

Boonvisut, P., Çavuşoğlu, M.C., 2013. Estimation of soft tissue mechanical parameters from robotic manipulation data. IEEE/ASME Transactions on Mechatronics 18, 1602–1611.

Buffinton, C.M., Tong, K.J., Blaho, R.A., Buffinton, E.M., Ebenstein, D.M., 2015. Comparison of mechanical testing methods for biomaterials: Pipette aspiration, nanoindentation, and macroscale testing. Journal of the Mechanical Behavior of Biomedical Materials 51, 367–379.

Cecchi, R., Verotti, M., Capata, R., Dochshanov, A., Broggiato, G.B., Crescenzi, R., Balucani, M., Natali, S., Razzano, G., Lucchese, F., Bagolini, A., Bellutti, P., Sciubba, E., Belfiore, N.P., 2015. Development of microgrippers for tissue and cell manipulation with direct morphological comparison. Micromachines 6, 1710–1728.

Chang, H., Zhao, H., Ye, F., Yuan, G., Xie, J., Kraft, M., Yuan, W., 2014. A rotary comb-actuated microgripper with a large displacement range. Microsystem Technologies 20, 119–126.

Chawla, A., Mukherjee, S., Karthikeyan, B., 2009. Characterization of human passive muscles for impact loads using genetic algorithm and inverse finite element methods. Biomechanics and modeling in mechanobiology 8, 67–76.

Chen, K., Yao, A., Zheng, E.E., Lin, J., Zheng, Y., 2012. Shear wave dispersion ultrasound vibrometry based on a different mechanical model for soft tissue characterization. Journal of Ultrasound in Medicine 31, 2001–2011.

Dao, S.D., Abhary, K., Marian, R., 2017. A bibliometric analysis of genetic algorithms throughout the history. Computers & Industrial Engineering 110, 395–403.

Di Giamberardino, P., Bagolini, A., Bellutti, P., Rudas, I.J., Verotti, M., Botta, F., Belfiore, N.P., 2018. New mems tweezers for the viscoelastic characterization of soft materials at the microscale. Micromachines 9.

Dochshanov, A., Verotti, M., Belfiore, N.P., 2017. A comprehensive survey on microgrippers design: operational strategy. Journal of Mechanical Design 139, 070801.

Eng, R.C., Sampathkumar, A., 2018. Getting into shape: the mechanics behind plant morphogenesis. Current opinion in plant biology 46, 25–31.

Erath, B.D., Zañartu, M., Peterson, S.D., 2017. Modeling viscous dissipation during vocal fold contact: the influence of tissue viscosity and thickness with implications for hydration. Biomechanics and modeling in mechanobiology 16, 947–960.

Esen, I., Koç, M.A., 2015. Optimization of a passive vibration absorber for a barrel using the genetic algorithm. Expert Systems with Applications 42, 894–905.

Ewins, D.J., 2009. Modal Testing: Theory, Practice and Application, 2nd Edition. John Wiley & Sons, Inc.

Forte, A.E., Galvan, S., Dini, D., 2018. Models and tissue mimics for brain shift simulations. Biomechanics and modeling in mechanobiology 17, 249–261.

Freed, A.D., Einstein, D.R., 2012. Hypo-elastic model for lung parenchyma. Biomechanics and modeling in mechanobiology 11, 557–573.

Garcés-Schröder, M., Metz, D., Hecht, L., Iyer, R., Leester-Schädel, M., Böl, M., Dietzel, A., 2018. Characterization of skeletal muscle passive mechanical properties by novel micro-force sensor and tissue micro-dissection by femtosecond laser ablation. Microelectronic Engineering 192, 70–76.

Haupt, R.L., Haupt, S.E., 1998. Practical genetic algorithms. volume 2. Wiley New York.

Hsu, C.K., Lin, H.H., Hans, I., Harn, C., Hughes, M., Tang, M.J., Yang, C.C., 2018. Mechanical forces in skin disorders. Journal of dermatological science .

Hu, S., Yang, C., Hu, D., Lam, R.H., 2017. Microfluidic biosensing of viscoelastic properties of normal and cancerous human breast cells, in: Nano/Micro Engineered and Molecular Systems (NEMS), 2017 IEEE 12th International Conference on, IEEE. pp. 90–95.

Huveneers, S., Daemen, M.J., Hordijk, P.L., 2015. Between rho (k) and a hard place: the relation between vessel wall stiffness, endothelial contractility, and cardiovascular disease. Circulation research 116, 895–908.

Ingber, D., 2003. Mechanobiology and diseases of mechanotransduction. Annals of medicine 35, 564–577.

Ji, B., Gao, H., 2004. Mechanical properties of nanostructure of biological materials. Journal of the Mechanics and Physics of Solids 52, 1963–1990.

Jin, X., Zhu, F., Mao, H., Shen, M., Yang, K.H., 2013. A comprehensive experimental study on material properties of human brain tissue. Journal of biomechanics 46, 2795–2801.

Johnson, M.L., Faunt, L.M., 1992. Parameter estimation by least-squares methods, in: Methods in enzymology. Elsevier. volume 210, pp. 1–37.

Kauer, M., Vuskovic, V., Dual, J., Székely, G., Bajka, M., 2002. Inverse finite element characterization of soft tissues. Medical Image Analysis 6, 275–287.

Kohandel, M., Sivaloganathan, S., Tenti, G., 2008. Estimation of the quasi-linear viscoelastic parameters using a genetic algorithm. Mathematical and Computer Modelling 47, 266–270.

Laksari, K., Assari, S., Seibold, B., Sadeghipour, K., Darvish, K., 2015. Computational simulation of the mechanical response of brain tissue under blast loading. Biomechanics and modeling in mechanobiology 14, 459–472.

Lim, C., Zhou, E., Quek, S., 2006. Mechanical models for living cells—a review. Journal of biomechanics 39, 195–216.

Marchi, B.C., Arruda, E.M., 2017. A study on the role of articular cartilage soft tissue constitutive form in models of whole knee biomechanics. Biomechanics and modeling in mechanobiology 16, 117–138.

Marcucci, L., Reggiani, C., Natali, A.N., Pavan, P.G., 2017. From single muscle fiber to whole muscle mechanics: a finite element model of a muscle bundle with fast and slow fibers. Biomechanics and modeling in mechanobiology 16, 1833–1843.

Mijailovic, A.S., Qing, B., Fortunato, D., Van Vliet, K.J., 2018. Characterizing viscoelastic mechanical properties of highly compliant polymers and biological tissues using impact indentation. Acta biomaterialia 71, 388–397.

Miller, K., Chinzei, K., 2002. Mechanical properties of brain tissue in tension. Journal of biomechanics 35, 483–490.

Murdock, K., Martin, C., Sun, W., 2018. Characterization of mechanical properties of pericardium tissue using planar biaxial tension and flexural deformation. Journal of the mechanical behavior of biomedical materials 77, 148–156.

Nguyen, A.V., Nyberg, K.D., Scott, M.B., Welsh, A.M., Nguyen, A.H., Wu, N., Hohlbauch, S.V., Geisse, N.A., Gibb, E.A., Robertson, A.G., et al., 2016. Stiffness of pancreatic cancer cells is associated with increased invasive potential. Integrative Biology 8, 1232–1245.

Pogoda, K., Chin, L., Georges, P.C., Byfield, F.J., Bucki, R., Kim, R., Weaver, M., Wells, R.G., Marcinkiewicz, C., Janmey, P.A., 2014. Compression stiffening of brain and its effect on mechanosensing by glioma cells. New journal of physics 16, 075002.

Prasadh, S., Wong, R.C.W., 2018. Unraveling the mechanical strength of biomaterials used as a bone scaffold in oral and maxillofacial defects. Oral Science International .

Rodriguez, M., Sniadecki, N., 2014. Computational modeling of cell mechanics, in: Computational Modelling of Biomechanics and Biotribology in the Musculoskeletal System. Elsevier, pp. 93–140.

Rodriguez, M.L., McGarry, P.J., Sniadecki, N.J., 2013. Review on cell mechanics: experimental and modeling approaches. Applied Mechanics Reviews 65, 060801.

Rubiano, A., Delitto, D., Han, S., Gerber, M., Galitz, C., Trevino, J., Thomas, R.M., Hughes, S.J., Simmons, C.S., 2018. Viscoelastic properties of human pancreatic tumors and in vitro constructs to mimic mechanical properties. Acta biomaterialia 67, 331–340.

Sanò, P., Verotti, M., Bosetti, P., Belfiore, N.P., 2018. Kinematic synthesis of a d-drive mems device with rigid-body replacement method. Journal of Mechanical Design 140, 075001.

Sato, M., Theret, D., Wheeler, L., Ohshima, N., Nerem, R., 1990. Application of the micropipette technique to the measurement of cultured porcine aortic endothelial cell viscoelastic properties. Journal of biomechanical engineering 112, 263–268.

Sherman, V.R., Tang, Y., Zhao, S., Yang, W., Meyers, M.A., 2017. Structural characterization and viscoelastic constitutive modeling of skin. Acta biomaterialia 53, 460–469.

Verotti, M., 2018. Effect of initial curvature in uniform flexures on position accuracy. Mechanism and Machine Theory 119, 106–118.

Verotti, M., Crescenzi, R., Balucani, M., Belfiore, N.P., 2015. Mems-based conjugate surfaces flexure hinge. Journal of Mechanical Design 137, 012301.

Verotti, M., Dochshanov, A., Belfiore, N., 2017a. A comprehensive survey on microgrippers design: mechanical structure. Journal of Mechanical Design 139, 060801.

Verotti, M., Dochshanov, A., Belfiore, N.P., 2017b. Compliance synthesis of CSFH MEMS-based microgrippers. Journal of Mechanical Design 139, 022301.

Vivanco, J., Aiyangar, A., Araneda, A., Ploeg, H.L., 2012. Mechanical characterization of injection-molded macro porous bioceramic bone scaffolds. Journal of the mechanical behavior of biomedical materials 9, 137–152.

Wang, F., Han, Y., Wang, B., Peng, Q., Huang, X., Miller, K., Wittek, A., 2018. Prediction of brain deformations and risk of traumatic brain injury due to closed-head impact: quantitative analysis of the effects of boundary conditions and brain tissue constitutive model. Biomechanics and modeling in mechanobiology , 1–21.

Weiner, S., Wagner, H.D., 1998. The material bone: structure-mechanical function relations. Annual Review of Materials Science 28, 271–298.

Whitford, C., Movchan, N.V., Studer, H., Elsheikh, A., 2018. A viscoelastic anisotropic hyperelastic constitutive model of the human cornea. Biomechanics and modeling in mechanobiology 17, 19–29.

Xi, J., Lamata, P., Lee, J., Moireau, P., Chapelle, D., Smith, N., 2011. Myocardial transversely isotropic material parameter estimation from in-silico measurements based on a reduced-order unscented kalman filter. Journal of the Mechanical Behavior of Biomedical Materials 4, 1090 – 1102. doi:https://doi.org/10.1016/j.jmbbm.2011.03.018.

Xu, W., Mezencev, R., Kim, B., Wang, L., McDonald, J., Sulchek, T., 2012. Cell stiffness is a biomarker of the metastatic potential of ovarian cancer cells. PloS one 7, e46609.

Zhang, W., Liu, L.f., Xiong, Y.j., Liu, Y.f., Yu, S.b., Wu, C.w., Guo, W., 2018. Effect of in vitro storage duration on measured mechanical properties of brain tissue. Scientific reports 8, 1247.

Zhou, Y., Bao, Z., Luo, Q., Zhang, S., 2017. A complex-valued encoding wind driven optimization for the 0-1 knapsack problem. Applied Intelligence 46, 684–702.

Zouaoui, J., Trunfio-Sfarghiu, A., Brizuela, L., Piednoir, A., Maniti, O., Munteanu, B., Mebarek, S., Girard-Egrot, A., Landoulsi, A., Granjon, T., 2017. Multi-scale mechanical characterization of prostate cancer cell lines: Relevant biological markers to evaluate the cell metastatic potential. Biochimica et Biophysica Acta (BBA)-General Subjects 1861, 3109–3119.